



# Design and synthesis of porous Ag/ZnO nanosheets assemblies as super photocatalysts for enhanced visible-light degradation of 4-nitrophenol and hydrogen evolution

Hongyu Mou<sup>a</sup>, Caixia Song<sup>a,\*</sup>, Yanhong Zhou<sup>b</sup>, Bo Zhang<sup>b</sup>, Debao Wang<sup>b,\*</sup>

<sup>a</sup> College of Materials Science and Engineering, Qingdao University of Science & Technology, Qingdao 266042, China

<sup>b</sup> Key Lab of Inorganic Synthetic and Applied Chemistry, State Key Lab Base of Eco-Chemical Engineering, College of Chemistry and Molecular Engineering, Qingdao University of Science & Technology, Qingdao 266042, China



## ARTICLE INFO

### Keywords:

Ag/ZnO  
Photocatalysis  
Photocatalytic degradation  
Hydrogen evolution  
Photoelectrochemical

## ABSTRACT

Three-dimensional (3D) Ag/ZnO assemblies with porous nanosheets as building blocks have been designed and selectively prepared via a facial solution method followed by topological morphology conversion with low temperature calcination. The samples were characterized thoroughly by using XRD, SEM, TEM, HRTEM, N<sub>2</sub> isotherms, UV-vis spectroscopy, PL, EIS, Mott-Schottky plots, and photocurrent response. The as-prepared 3D Ag/ZnO architectures were evaluated as photocatalysts for hydrogen evolution and organic pollutants removal from aqueous solution, which demonstrates superior sun-light driven photocatalytic activities to those of ZnO architectures. Nearly 100% photocatalytic degradation of 10 ppm 4-nitrophenol was obtained just for 25 min and 0.4436 mmol g<sup>-1</sup> h<sup>-1</sup> of hydrogen production rate was achieved over Ag/ZnO architectures. The photocurrent of the Ag/ZnO photoelectrode showed an enhancement of three times of ZnO architectures. The enhanced photocatalytic activity may be attributed to the synergistic effect between 2D ZnO porous single crystalline nanosheets and silver components, which could not only accelerate separation and migration efficiency of charge carries, but also enhance charge-collection efficiency.

## 1. Introduction

Due to the rapid development of the global economy, a series of energy and environmental problems have come into being. Sustainable energy supply and environmental protection are two of the most important issues in the development of the world [1]. Hydrogen is believed to be one of the most important clean fuels for the future. However, kick-starting the hydrogen economy will require cheap ways to produce mass quantities of hydrogen. Among the various hydrogen production technologies, semiconductor-based photocatalytic water splitting systems have received more attention because of their potential application in the direct production of clean hydrogen energy by using water and light (or ideally sunlight) [2,3]. For environmental remediation, photocatalytic technology, as an advanced oxidation process, has received much attention over the past few years [4,5]. Unlike the traditional physical techniques, photocatalytic technology provides a powerful oxidation process used for the removal of organic contaminants by completely converting them into CO<sub>2</sub> and H<sub>2</sub>O, and thus no hazardous breakdown products will be left [6].

Development of the sunlight-driven photocatalysts is an effective

and promising way to meet both energy demands and water pollution issues. Among all the known photocatalysts, semiconductor ZnO has been extensively studied due to its non-toxicity and good photocatalytic and photoelectrochemical properties. However, ZnO is a wide band gap (3.37 eV) semiconductor with a large excitonic binding energy (60 meV), and as a result, two issues limit the industrial-scale use of ZnO [7]: one is that ZnO absorbs photons only in the UV region (below 400 nm), which suffer from limitations for sunlight-driven photocatalysts; the other is that ZnO has a rapid recombination rate of photogenerated electrons (e<sup>-</sup>) and holes (h<sup>+</sup>), as a result, its UV activity is not high enough from a viewpoint of practical applications.

To overcome these two drawbacks, many new photocatalytic systems based on ZnO have been developed over the past few decades including the control of the morphology [8], cationic or anionic doping [9,10], composite [11], and modifying the surface with noble metal nanoparticles [12], among which, noble metal hybridized ZnO is recognized as a promising candidate photocatalytic system. Of the noble metal investigated, Ag is attracted much attention due to its low cost, non-toxicity, high electrical and thermal conductivity. Therefore, a series of Ag/ZnO nanocomposites with different morphologies, such as

\* Corresponding authors.

E-mail addresses: [songcaixia@qust.edu.cn](mailto:songcaixia@qust.edu.cn) (C. Song), [dbwang@qust.edu.cn](mailto:dbwang@qust.edu.cn) (D. Wang).

nanoparticles [13,14], microrods [15], pompon-like [16], hollow microspheres [17], and flower-like ZnO microstructures [18–20], have been prepared through various methods. However, the design and preparation of photocatalysts with higher activity are still required.

Recently, engineering defects and micropores in 2D photocatalysts has been identified to be an effective way to obtain high catalytic activity [21,22]. Herein, we report the design and synthesis of porous Ag/ZnO nanosheets assemblies with self-assembled 3D structures. The surface-engineered Ag/ZnO ultrathin nanosheets exhibit single crystalline natures with abundant pores and are decorated with highly dispersed Ag nanospecies. The microscale architectures are benefit for preventing the aggregation of the nanosheets while retaining merits of the primary nanosheet subunits. As expected, by the effective design and surface engineering, high-performance Ag/ZnO photocatalysts for organic pollutants removal and hydrogen evolution were achieved.

## 2. Experimental

### 2.1. Synthesis of photocatalysts

All chemicals are analytical grade and were used without further purification. In a typical procedure, 1.275 mmol zinc acetate, 0.4 g urea, and 0.025 mmol potassium sodium tartrate was dissolved in 50 mL of deionized water at room temperature, then calculated amount of silver nitrate was added under stirring. The solution was heated at 90 °C for 12 h in an electronic oven. After the reaction, the brown precursor precipitates were centrifuged and washed thoroughly with ethanol and water, respectively, and then, were dried at 60 °C. Finally, the precursor was calcined at 300 °C for 0.5 h in air atmosphere to obtain Ag/ZnO hierarchical microspheres. ZnO hierarchical structures were prepared following the same procedure in the absence of silver nitrate.

### 2.2. Characterization

The powder X-ray diffraction (XRD) patterns were recorded on a D/max-2500/PC X-ray diffractometer with Cu K $\alpha$  radiation ( $\lambda = 1.5405981 \text{ \AA}$ ). Scanning electron microscopy (SEM) images were taken on a JSM-6700F field emission scanning electron microscope. Transmission electron microscopy (TEM) images and high-resolution TEM (HRTEM) images were performed on a JEOL JEM-2010 high-resolution transmission electron microscope operated at 200 kV. Specific surface areas and pore size distribution were analyzed on Micromeritics ASAP 2020 N<sub>2</sub> adsorption analyzer using the BET (Brunauer-Emmet-Teller) and BJH (Barrett-Joyner-Halenda) methods, respectively. UV-vis diffuse reflectance spectra (DRS) were obtained on a Model c spectrophotometer equipped with an integrating sphere using BaSO<sub>4</sub> as the reflectance standard. The photoluminescence spectra (PL) were recorded with a Perkin Elme LS-55 spectrophotometer excited with a 325 nm wavelength. X-ray photoelectron spectra (XPS) were

recorded using a Thermo ESCALAB 250XI multifunctional imaging electron spectrometer with Al K $\alpha$  radiation ( $h\nu = 1486.6 \text{ eV}$ ) at 150 W. The binding energy of the C 1s line at 284.8 eV was used as an internal standard reference.

### 2.3. Photocatalytic degradation of 4-nitrophenol (4-NP)

The photocatalytic performance of the Ag/ZnO architectures was evaluated via the photocatalytic degradation of 4-nitrophenol (4-NP). A 300 W xenon lamp was used as a light source and the light density was adjusted to 100 mW cm<sup>-2</sup>. In a typical procedure, the 30 mg of photocatalysts were dispersed in 100 mL of 10 ppm 4-NP solutions. The suspensions were stirred in the dark for 0.5 h to reach an adsorption-desorption equilibrium. Then the suspensions were subsequently exposed to visible-light irradiation under continuous stirring, 3 mL aliquots were extracted out at regular intervals and centrifuged to remove Ag/ZnO architectures. The collected 4-NP solution was eventually analyzed by using a PerkinElmer Lambda750 spectrophotometer.

### 2.4. Photocatalytic hydrogen evolution

Typically, 30 mg of the photocatalysts were dispersed into 100 mL of aqueous solution containing 0.25 M Na<sub>2</sub>S and 0.35 M Na<sub>2</sub>SO<sub>3</sub> in a pyrex reactor with a magnetic stirrer. A 300 W xenon lamp with intensity of 100 mW/cm<sup>2</sup> was applied as light source, which was positioned on the top of photoreactor. The irradiation time was 24 h. The hydrogen product from the aqueous solution was analyzed by gas chromatography (GC-7920). The carrier gas was high purity nitrogen.

### 2.5. Electrochemical analysis

All the electrochemical and photoelectrochemical (PEC) measurements were carried out on a Princeton Applied Research ParStat 2273 using a three-electrode system with a Pt/Nb wire as the counter electrode, saturated calomel electrode (SCE) as the reference electrode, and the as-prepared photoanodes as the working electrode. The Mott-Schottky (MS) plots were measured in a 0.5 M KPi buffer (pH 7) at a frequency of 1000 Hz and amplitude of 10 mV under the dark condition. Electrochemical impedance spectroscopy (EIS) was carried out in the frequency range of 0.5 Hz–105 KHz, with AC voltage amplitude of 10 mV in a 0.5 M Na<sub>2</sub>SO<sub>4</sub> aqueous solution. For photocurrent density vs. potential (j-v) and photocurrent density vs. time (j-t) curves, the working electrode with an area of 1 × 1 cm<sup>2</sup> was immersed in 0.5 M Na<sub>2</sub>SO<sub>4</sub> aqueous solution and illuminated using a 300 W Xe-lamp with a light density of 100 mW cm<sup>-2</sup> at 0.0 V versus SCE.

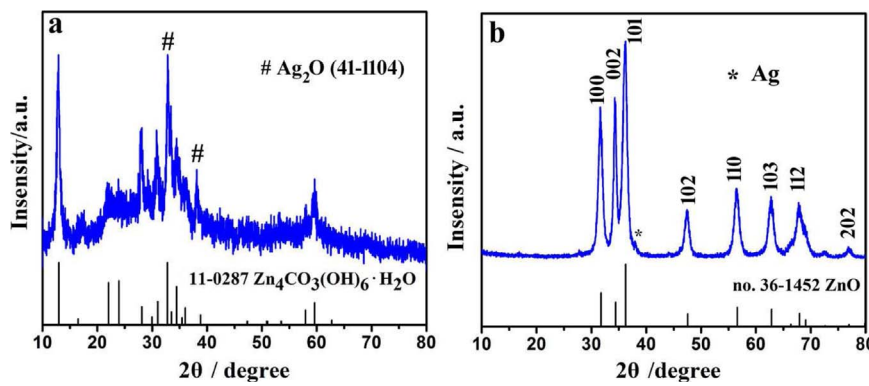


Fig. 1. XRD patterns of the precursor (a) and after calcination (b).

### 3. Results and discussion

#### 3.1. XRD analysis

**Fig. 1** illustrates the XRD patterns of the precursor and Ag/ZnO sample obtained after calcination. In **Fig. 1(a)**, most of the diffraction peaks can be indexed to those of zinc carbonate hydroxides, such as  $\text{Zn}_4\text{CO}_3(\text{OH})_6\text{H}_2\text{O}$  according to JCPDS File no. 11–287 and the peaks marked with # can be assigned to  $\text{Ag}_2\text{O}$  (JCPDS File no. 41–1104), which indicates the precursor contains mainly zinc carbonate hydroxides  $\text{Zn}_4\text{CO}_3(\text{OH})_6\text{H}_2\text{O}$  and the loading  $\text{Ag}_2\text{O}$ . Diffraction peaks in **Fig. 1b** can be indexed to the wurtzite structure  $\text{ZnO}$  (JCPDS File No. 36–1451) together with that of metal Ag marked with an asterisk (JCPDS File no. 65–2871), which confirms the phase transformation of zinc carbonate hydroxides and  $\text{Ag}_2\text{O}$  to form Ag/ZnO sample after calcining the precursors and the diffraction peaks were labelled in **Fig. 1b**. In addition, the relative intensity of (002) peak of  $\text{ZnO}$  becomes much stronger than that of the standard pattern indicating the (002) oriented growth of  $\text{ZnO}$ . The sharp and strong diffraction peaks indicate the high crystalline nature of  $\text{ZnO}$ , which in turn suppresses the relative intensity of Ag diffraction.

#### 3.2. SEM and HRTEM analysis

SEM image in **Fig. 2a** clearly reveals that the precursor is composed of well dispersed hierarchical microspheres with diameters of 4–5  $\mu\text{m}$ , which are assembled with nanosheets. After calcination, as shown in **Fig. 2b,c**, the morphologies of the Ag/ZnO assembled architectures maintain well. A detailed observation of an individual Ag/ZnO microsphere is shown **Fig. 2c**, it is obvious that  $\text{ZnO}$  nanosheets are flexible and have a thickness of about 20 nm. **Fig. 2d** shows typical TEM image of the nanosheets from the Ag/ZnO assemblies, in which the nanosheets are composed of overlapped and translucent layers with porous feature. A close and detailed identification of the microstructures of the nanosheets was further conducted by HRTEM. It can be seen from **Fig. 2e–g**

that continuous lattice fringes were observed as a whole, clearly indicating their single-crystalline nature. Some disordered mesopores can also be observed. Ag nanoparticles with sizes of ca. 5 nm can also be found being anchored on the nanosheets as circled in zone 1. The enlarged image of zone 1 in **Fig. 2f** shows d-spacing of 0.24 nm corresponding to (111) planes of metal silver. The d-spacing of 0.26 nm in **Fig. 2g** belongs to (002) planes of  $\text{ZnO}$ , and a typical edge dislocation is also observed in **Fig. 2g** (circled zone in **Fig. 2g**). The HRTEM results are consistent with XRD analysis. The unique single crystalline structure can provide direct 2D electron channels for photogenerated charges fast transporting through the nanosheet to accelerate the charge separation and electron transport [21].

#### 3.3. XPS analysis

XPS analyses were conducted to further analyze the surface composition and chemical states of Ag/ZnO assembled architectures. **Fig. 3a** shows the Gauss fitting curves of the O 1 s spectra, which implies the presence of two different kinds of O species. The main species of the lower binding energy located at 530.7 eV can be attributed to the lattice oxygen of  $\text{ZnO}$ . While the higher binding energy species centered at around 532 eV is associated with the chemisorbed oxygen of the surface oxygen species and hydroxyls in the surface deficiency regions such as oxygen vacancy ( $\text{V}_\text{O}$ ), oxygen interstitial ( $\text{O}_\text{i}$ ), and oxygen antisite ( $\text{O}_{\text{Zn}}$ ) [13,23,24]. It has been proven that the surface oxygen and hydroxyls are capable of trapping photogenerated electrons and holes resulting in the formation of hydroxyl radical species ( $\cdot\text{OH}$ ) which are significant for photocatalytic reaction, as will be discussed later. In addition, no obvious peak is observed in **Fig. 3a** at the binding energy of about 529.0 eV, which attributes to lattice O in  $\text{Ag}_2\text{O}$  and suggests that the presence of silver is Ag (0) [18].

**Fig. 3b** exhibits the high-resolution spectra of Zn 2p state, the doublet peaks at 1021 and 1044 eV are associated with the binding energy of Zn 2p<sub>3/2</sub> and Zn 2p<sub>1/2</sub>, respectively. This infers that Zn only exists in a divalent oxidation state in the samples [25]. **Fig. 3c** presents

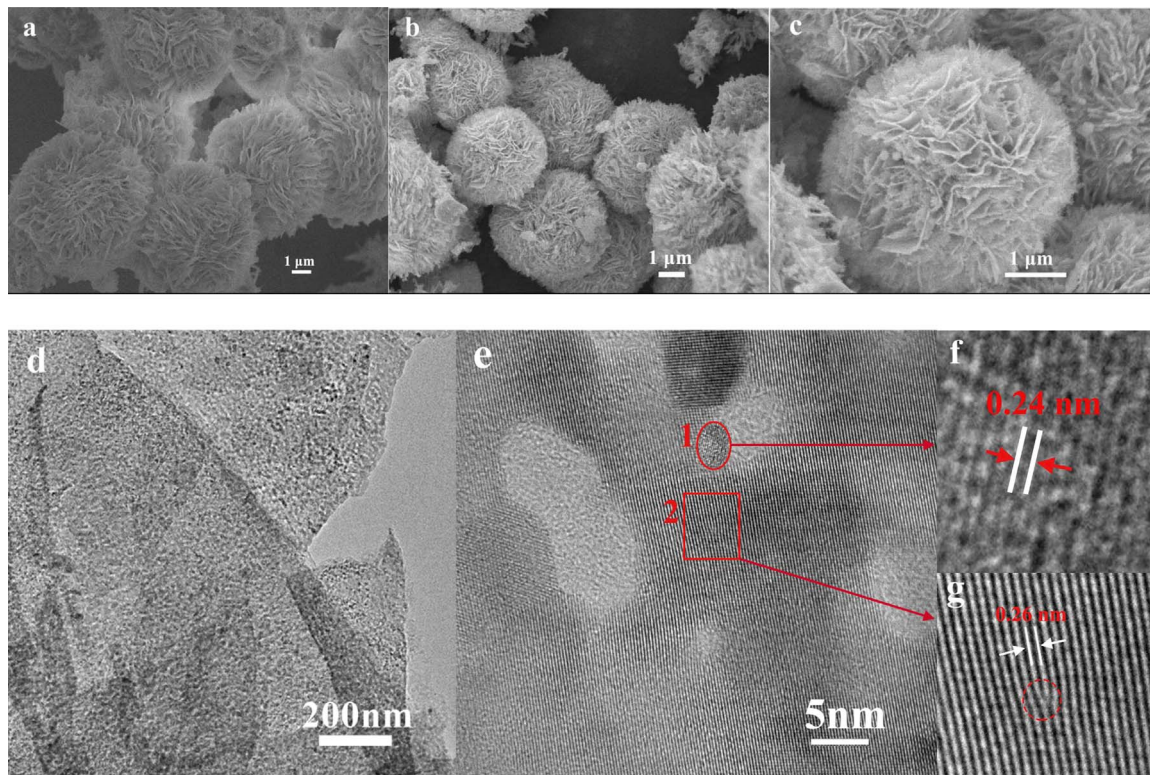


**Fig. 2.** SEM images of the precursor (a) and Ag/ZnO (b,c), and TEM (d) and HRTEM (e–g) images of Ag/ZnO sample.

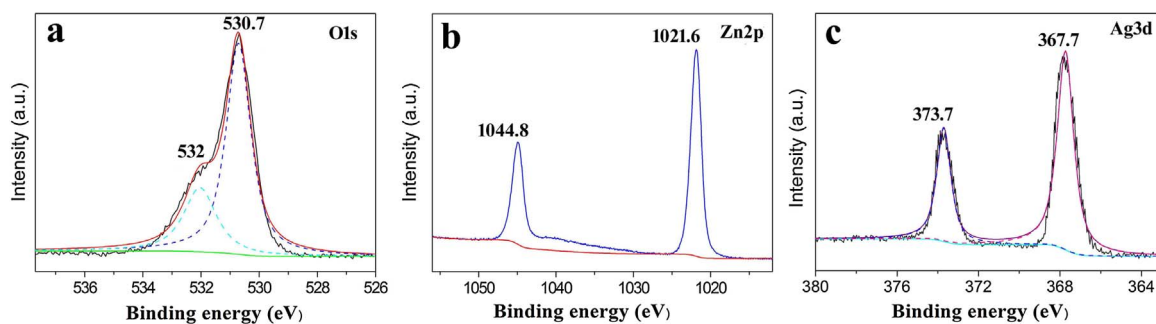


Fig. 3. XPS spectra of Ag/ZnO sample: (a) O1s, (b) Zn 2p, and (c) Ag 3d.

the binding energies of Ag 3d5/2 and Ag 3d3/2 located at 367.7 and 373.7 eV, respectively, with the splitting of 6 eV. The measured spectra shift slightly to lower binding energy comparing with the corresponding values of the bulk Ag locating at about 368.2 and 374.2 eV, respectively [26]. The binding energy shift of Ag 3d has been mainly attributed to the electron transfer between metallic Ag and ZnO nanocrystal, and similar results have been reported in the literature for Ag/ZnO nanostructures [13,23,27,28]. When the Ag nanoparticles and ZnO nanosheets attach together, they will adjust the position of their corresponding Fermi energy to a new level. And the free electrons will transfer from Ag to the conduction band of ZnO nanosheets. The formation of Schottky barrier at metal-semiconductor interface between the Ag and ZnO further improves the segregation of charges and prevents the charge recombination. As a result, the free electrons transferring was enhanced and the electron density of Ag is decreased, indicating the significant positive charge of Ag. Though XRD of Ag/ZnO sample shows the presence of Ag (0) state only, slight oxidation of Ag cannot be ruled out because of the lower binding energy of Ag (1) than that of Ag (0) [29]. In addition, the calculated silver content is PP At. 3.12%.

#### 3.4. Nitrogen isotherm

The nitrogen adsorption-desorption isotherms and pore size distribution plots have been applied to further analyze the microstructures of the Ag/ZnO architectures. As shown in Fig. 4, the isotherm displays the typical type IV curve, which indicates the characteristics of a mesoporous structure. The BJH pore size distribution is determined from the desorption branch of the isotherm. As shown in the inset of Fig. 4, most of the pores possess diameters in the range of 2–60 nm with two peak zeniths centering around 3 nm and 25 nm, respectively, which further confirms the mesoporous nature of the Ag/ZnO sample in agreement with the HRTEM results. The specific surface area calculated by BET method is 43.2 m<sup>2</sup>/g for Ag/ZnO architecture. Table 1

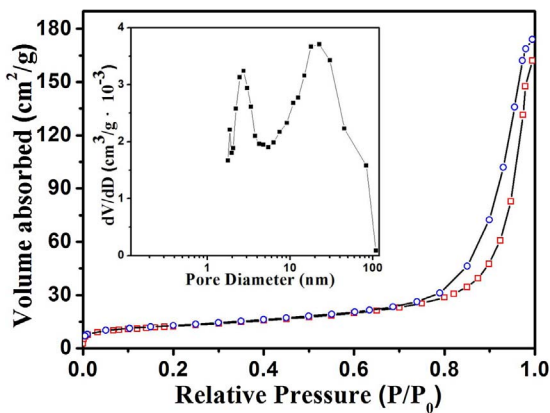


Fig. 4. Nitrogen adsorption-desorption isotherm and pore size distribution (inset) of Ag/ZnO architectures.

Table 1

BET surface areas of Ag/ZnO architecture in this work and relevant literature reports.

Catalyst	BET surface area (m <sup>2</sup> /g)	Ref.
Ag/ZnO architectures	43.2	this work
Porous Ag/ZnO flower-like	34.3	[28]
Ag/ZnO particles	3.5	[30]
Nanoporous Ag/ZnO microrods	20.9	[31]
Nano Ag/ZnO	4.2	[32]
Flower-like ZnO architectures	27.43	[33]

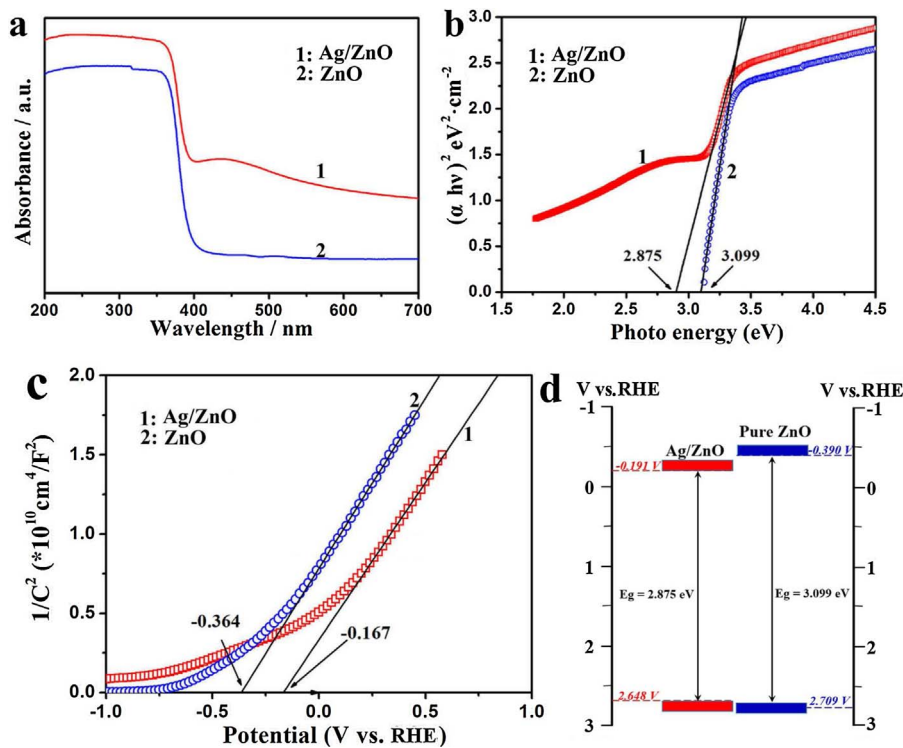
summarizes the calculating BET surface area values of the synthesized Ag/ZnO architectures and those of the relevant literature reports for comparison. It is evident that the as-prepared Ag/ZnO architectures possess much higher specific area.

#### 3.5. Band gap analysis

DRS analysis and MS plots were carried out to investigate the effect of modification Ag on the optical absorption and band potentials of the Ag/ZnO architectures. As shown in Fig. 5a, an SPR absorption peak at 450 nm can be found for Ag/ZnO architectures comparing with that of pure ZnO. The expansion of the absorption from UV to visible area compared with that of ZnO suggests potential application of Ag/ZnO architectures as visible light derived photocatalyst [34,35]. The energy band gap of the samples was estimated to be 3.099 eV and 2.875 eV for ZnO and Ag/ZnO architectures, respectively, from the variation of  $(\alpha h\nu)^2$  with  $h\nu$  (Fig. 5b).

In order to further understand the band structure of Ag/ZnO, the Mott-Schottky (MS) plots of both ZnO and Ag/ZnO architectures electrodes are depicted in Fig. 5c. Both of the samples exhibit positive slopes, indicating Ag/ZnO hybrid architectures still maintain n-type semiconductor. The carrier density and flatband potentials can be deduced by the Mott-Schottky equation [36,37],  $1/C^2 = (2/A^2 qee_0 N_d) (V - V_{fb} - kT/q)$ . The flatband potentials can be estimated from the extrapolation of  $1/C^2 = 0$  in the plot of  $(1/C^2)$  versus  $V$ ,  $V_{fb} = V - kT/q$ , and are determined to be  $-0.390$  V and  $-0.191$  V for ZnO and Ag/ZnO architectures, respectively. The slope determined from the MS plot is used to estimate the carrier density using the equation,  $N_d = (2/qee_0) [d(1/C^2)/dV]^{-1}$ , and is calculated as  $8.2 \times 10^{18} \text{ m}^{-3}$  for Ag/ZnO. The density of states in the conduction band edge is expressed by  $N_c = 2(2\pi m^* kT/h^2)^{3/2}$ , and its value was calculated to be  $3.5 \times 10^{18} \text{ cm}^{-3}$  for Ag/ZnO architectures at room temperature. Thus, we can calculate the Schottky barrier height of Ag/ZnO architectures using  $\Phi_B = V_{fb} + (kT/q)\ln(N_c/N_d)$  to be  $\Phi_B = 0.17$  eV, which will improve the separation of photogenerated carriers, and then, enhance the photocatalytic activity.

It is accepted that the flat band potential is very close to the conduction band (CB) potential. Based on the results of above optical and electrochemical analyses, the electronic band structure of ZnO and Ag/ZnO architectures can be illustrated in Fig. 5d. Notably,  $E_{CB}$  of the Ag/ZnO architectures is more positive than that of the ZnO. The analysis



results are consistent with the DRS results.

### 3.6. PL spectra

PL spectra are recorded to study the charge generation, separation, and recombination properties of ZnO and Ag/ZnO photocatalysts. Fig. 6 shows the room-temperature PL spectra of the ZnO and Ag/ZnO architectures with an excitation wavelength of 325 nm. It can be seen that both of the two spectra cover the blue and green regions. Generally, the visible PL emission is attributed to different intrinsic defects, such as oxygen vacancies, zinc vacancies, oxygen interstitials, and zinc interstitials [38], which allows for increased light absorption and facilitates carrier separation and transportation [39,40]. With the loading of Ag to ZnO, the PL emission intensity decreases significantly, implying that Ag nanoparticles can increase the separation of photoexcited charge carrier and prevent the recombination of electron–hole pairs, which benefits the photocatalytic performance of Ag/ZnO architectures [41].

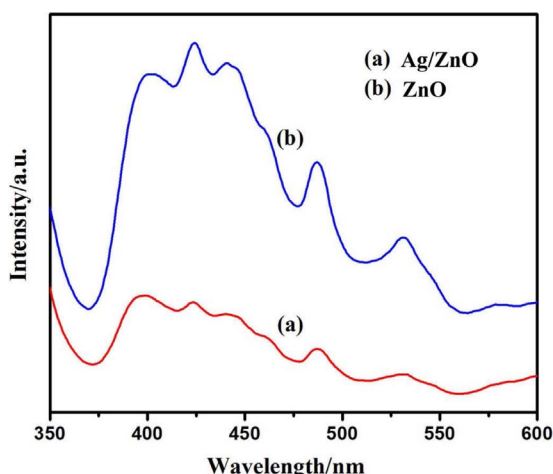


Fig. 6. PL spectra of ZnO and Ag/ZnO architectures.

Fig. 5. UV-vis DRS(a), the plot of  $(\alpha h\nu)^2$  versus  $h\nu$  (b), Mott-Schottky plots (c), and a schematic illustration of the band structures (d) of the photocatalysts.

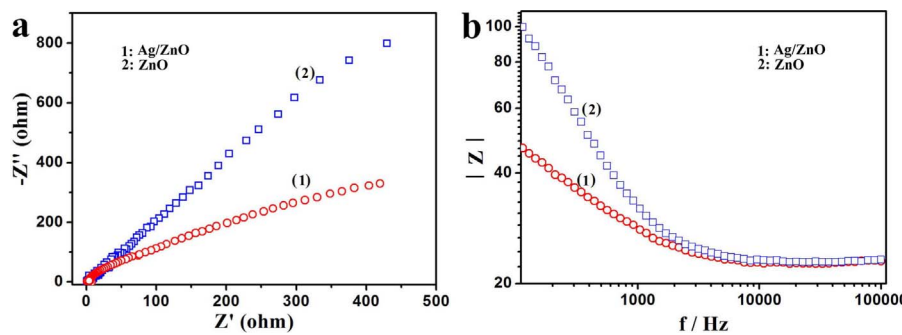
### 3.7. Electrochemical analysis

EIS Nyquist plots were employed to research the charge generation and transfer properties of the as-prepared photocatalysts. Fig. 7a shows the EIS Nyquist plots of ZnO and Ag/ZnO electrodes in 0.5 M Na<sub>2</sub>SO<sub>4</sub> aqueous solution. The radius of the arc on the EIS spectra reveals the interface layer resistance occurring at the surface of electrode, and a smaller radius always represents smaller charge transfer resistance [42]. It is observed that the arc radius of the Ag/ZnO (inset of Fig. 7a) is much smaller than that of ZnO, which indicates more rapid charge transfer in the Ag/ZnO architectures. Bode plots in Fig. 7b shows much lower |Z| value for Ag/ZnO electrodes than that of ZnO. Considering that the lower |Z| value implies easier charge transfer, it further confirms that the loading silver species can remarkably promote the charge transfer property of ZnO. These results demonstrate that the loading of Ag nanospecies to ZnO has dramatically enhanced the transportation rate of surface electrons through an interfacial interaction between ZnO nanosheets and the Ag nanospecies [43], which suggests higher photocatalysis activities can be achieved.

### 3.8. Photocatalytic degradation of 4-NP

The photocatalytic performance of the ZnO and hierarchical Ag/ZnO porous architectures were evaluated with simulated sun-light irradiation, and 4-NP was used as a representative organic pollutant for photocatalytic degradation. Fig. 8a shows UV-vis absorption spectra of 4-NP aqueous solution at different time intervals with Ag/ZnO architectures. The results showed that the main band of 4-NP at 402 nm obviously decrease with illumination times increasing and disappear completely just for 25 min irradiation. Fig. 8b shows the relative concentrations of 4-NP remaining in the solution as a function of the irradiation time with different photocatalysts. It can be seen that no obvious degradation of 4-NP can be observed for the absence of photocatalyst. The photocatalytic degradation rate is less than 80% for pure ZnO, while nearly 100% degradation has been achieved after being irradiated for 25 min using Ag/ZnO architectures.

Fig. 8c shows the photocatalytic degradation curves of 4-NP in the



form of  $-\ln(C_t/C_0)$  as a function of irradiation time, where  $C_0$  is the initial concentration of 4-NP and  $C_t$  presents the concentration remaining in the solution after irradiation time  $t$ . A linear relationship can be found between  $-\ln(C_t/C_0)$  and  $t$ , and the photocatalytic reaction kinetics can be described using the pseudo-first-order kinetics plot as  $-\ln(C_t/C_0) = k t + A$ , where  $k$  is a pseudo-first-order kinetics constant, which can be determined by linear fitting for different reactions. It is evident that the  $k$  value for degradation without photocatalyst is negligible ( $k = 3.60 \times 10^{-4} \text{ min}^{-1}$ ), and that Ag/ZnO architectures display the best photocatalytic activity with a  $k$  value of  $0.1305 \text{ min}^{-1}$  that is 2.4 times as large as that of pure ZnO ( $0.05561 \text{ min}^{-1}$ ). The enhancement of photocatalytic activity of Ag/ZnO under visible light irradiation results from the synergistic effect between Ag and ZnO and the surface plasmon resonance of Ag nanoparticles in Ag/ZnO architectures [44].

To investigate the stability and recycle photocatalytic performance of the as-prepared Ag/ZnO architectures, photocatalytic degradation 4-NP is cycled for five times and the results are shown in Fig. 8d. After each run, the Ag/ZnO photocatalyst was recycled by centrifuging, washing, and drying and was used for the next run. As can be seen from Fig. 8d, no obvious decrease in photocatalytic degradation performance can be found after five cycles, which demonstrates that the Ag/ZnO architectures have high photocatalyst stability and excellent reusability. The stability and activity may result from the micro/nanostructure characteristics of the as-prepared Ag/ZnO photocatalyst. The self-assembled microscale hierarchical structures are beneficial for

preventing the aggregation of the nanosheets while retaining merits of the primary subunits. Therefore, the unique structure exhibits enhanced activity and excellent stability in the photocatalytic process.

### 3.9. Free radical and hole trapping experiments

In order to further understand the mechanism on the enhanced photocatalytic activity, free radical and hole trapping experiments have been conducted to investigate the contributions of reactive species involved in the process of 4-NP degradation and the corresponding results are shown in Fig. 9. The scavengers used are methanol for hole ( $\text{h}^+$ ), benzoquinone(BQ) for superoxide radical ( $\cdot\text{O}_2^-$ ), and isopropanol (IPA) for hydroxyl radical ( $\cdot\text{OH}$ ). The photocatalytic degradation rates of 4-NP over Ag/ZnO decrease dramatically when BQ as an  $\cdot\text{O}_2^-$  scavenger was added into the photoreaction system, and a similar remarkable decrease was observed upon the addition of IPA as  $\cdot\text{OH}$  scavenger compared with no scavenger under similar conditions. While methanol as a scavenger of  $\text{h}^+$  only has minimal influence on the 4-NP degradation rate. Therefore, it can be concluded that  $\cdot\text{O}_2^-$  and  $\cdot\text{OH}$  are the predominant active species in the photocatalytic process of 4-NP degradation confirming that the dissolved  $\text{O}_2$  and  $\text{H}_2\text{O}$  molecules have significant influence on the photodegradation process.

### 3.10. Photocatalytic $\text{H}_2$ production

The as-prepared Ag/ZnO nanosheets assemblies have also been

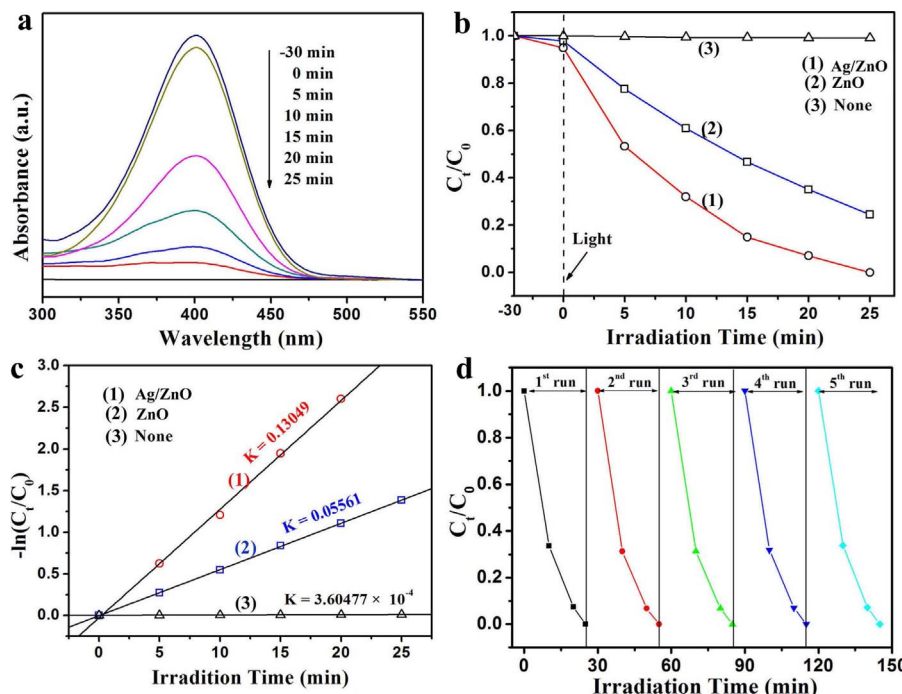


Fig. 8. (a) UV-vis absorption spectra of 4-NP at different time intervals with Ag/ZnO. (b) photocatalytic activity and (c) kinetics of 4-NP degradation with Ag/ZnO and ZnO. (d) Recycle photocatalytic degradation performance of Ag/ZnO for 4-NP.

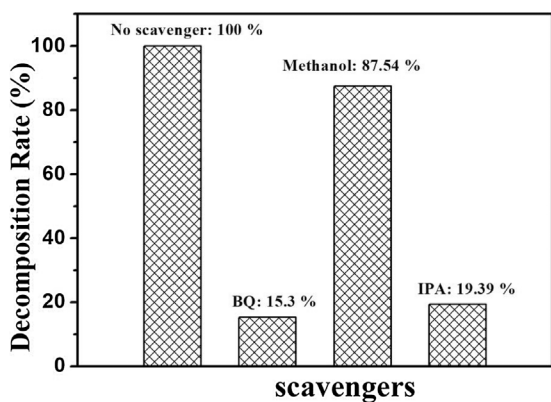


Fig. 9. Photocatalytic degradation rate of 4-NP over Ag/ZnO in the presence of scavengers.

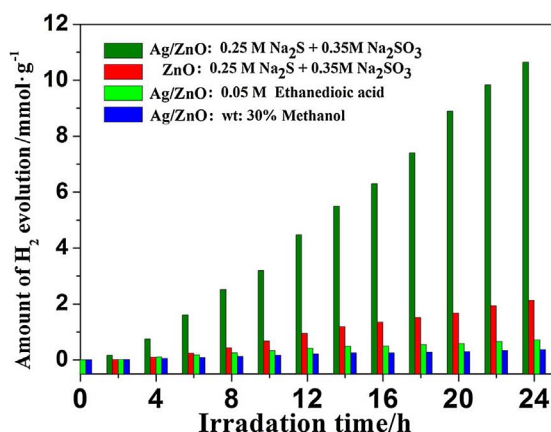


Fig. 10. Time-dependent photocatalytic H<sub>2</sub> production over Ag/ZnO and ZnO photo-catalysts with different sacrificial reagents.

Table 2  
Photocatalytic H<sub>2</sub> production of Ag/ZnO and those of relevant literature reports.

Photocatalyst	hydrogen production ( $\mu\text{mol h}^{-1} \text{g}^{-1}$ )	sacrificial reagents	Ref.
Ag/ZnO nanosheets assemblies	443.6	Na <sub>2</sub> S/Na <sub>2</sub> SO <sub>3</sub>	This work
Au/ZnO	427	ethanol	[45]
ZnO/ZnS heterostructures	384	glycerol	[46]
g-C <sub>3</sub> N <sub>4</sub> /ZnO (1.0 wt% Pt)	322	triethanolamine	[24]
ZnO/Zn <sub>x</sub> Cd <sub>1-x</sub> Te	265	Na <sub>2</sub> S/Na <sub>2</sub> SO <sub>3</sub>	[47]

evaluated as photocatalysts for photocatalytic water splitting hydrogen production (Fig. 10). It can be seen from Fig. 10 that as high as 10.7 mmol g<sup>-1</sup> (0.4436 mmol g<sup>-1</sup> h<sup>-1</sup>) of hydrogen production rate can be obtained over Ag/ZnO using Na<sub>2</sub>S/Na<sub>2</sub>SO<sub>3</sub> as sacrificial reagents. While the hydrogen production rate of pure ZnO is only about 0.0887 mmol g<sup>-1</sup> h<sup>-1</sup>, which demonstrates that the photocatalytic activity of ZnO can be greatly enhanced by loading silver nanospecies as co-catalyst and using Na<sub>2</sub>S/Na<sub>2</sub>SO<sub>3</sub> as sacrificial reagents. Table 2 summarizes the hydrogen production activities of the Ag/ZnO nanosheets assemblies in this work and the comparison with the relevant literature reports. It can be noticed that the H<sub>2</sub> production rate obtained in this work is higher than some of the ZnO based photocatalysts. The enhanced visible light photocatalytic H<sub>2</sub> production over the Ag/ZnO nanosheets assemblies should also be attributed to the unique microstructures.

Control experiments have been carried out to investigate the influence of sacrificial reagents on the hydrogen production rate. Fig. 10 also shows the hydrogen production rate over Ag/ZnO using oxalic acid and methanol as sacrificial reagents, respectively. It is evident that no obvious hydrogen production can be obtained when oxalic acid or methanol was used as sacrificial reagent, indicating preferred sacrificial reagents contribute greatly to the H<sub>2</sub> production activity of the photocatalysts.

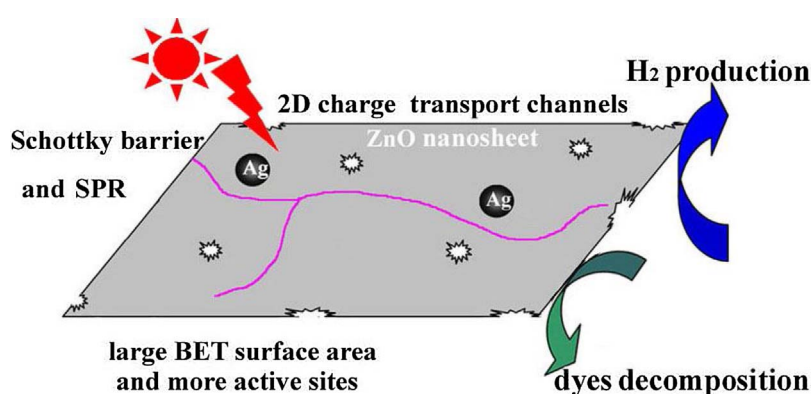
### 3.11. Photocatalytic mechanism

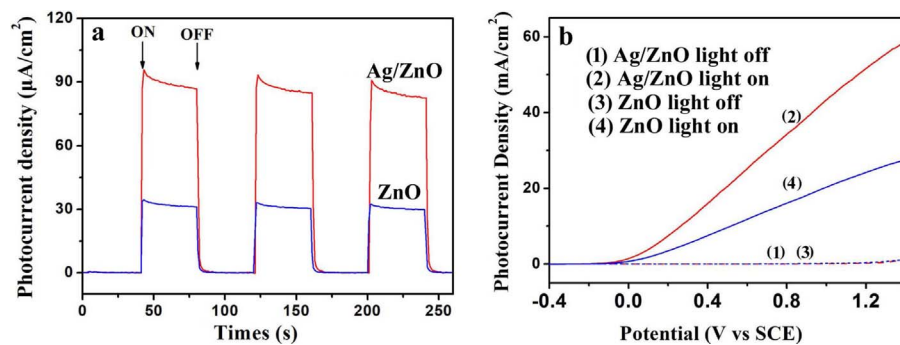
Based on the experimental results and discussions above, the mechanisms of the enhanced photocatalytic performance of Ag/ZnO architectures are illustrated in a diagram in Fig. 11. The enhanced photocatalytic activity of Ag/ZnO can be attributed to its unique architecture structures. The decoration of Ag nanospecies on the surface of ZnO nanosheets improves the segregation of charges and reduces the recombination of photo-induced electrons and holes due to the formation of the Schottky barrier at metal-semiconductor interface between Ag and ZnO nanosheets [48]. And the surface plasmon resonance (SPR) effect of Ag nanospecies can enhance the visible light absorption performance [49]. The single crystalline nature of the ZnO nanosheets provide direct electrical pathway for photogenerated charges smoothly walking along 2D channels to accelerate the generated electron-holes separation and electron transport. Moreover, the unique structure provides more active sites for enhanced photocatalytic performance. In addition, the meso-porosity of Ag/ZnO architectures provides buffer effect to avoid structure collapse of the nanosheets for high photocatalytic stability in long-term solution operation and endows large surface area which is beneficial for diffusion and adsorption of molecules to the surface of photocatalysts [21].

### 3.12. Photoelectrochemical (PEC) property

Photocurrent response measurements were carried out to confirm

Fig. 11. A diagram of the photocatalytic mechanism of the Ag/ZnO architectures.





the photoexcited charge generation of the as-prepared photocatalysts. Amperometric j-t studies were performed to examine the photoresponse of the Ag/ZnO and ZnO photoelectrodes over time. Fig. 12a shows J-t curves at 0 V versus SCE with the light on and off. The data show almost no dark currents for two photoelectrodes. Under illumination with light, the photocurrents increase sharply, indicating that the generation and separation of photoexcited electron-hole pairs is exceedingly high. This is also consistent with the electrochemical impedance spectra (EIS) results in Fig. 7. It can also be deduced that the Ag/ZnO architecture photoelectrode is relatively stable in the PEC water splitting process in a mild  $\text{Na}_2\text{SO}_4$  aqueous solution. A comparison in photocurrent density-potential (j-v) performance was shown in Fig. 12b. It is evident that the dark-current densities of Ag/ZnO and ZnO photoelectrodes are almost zero (curve 1,3), and upon illumination, both photoelectrodes exhibit much evident photocurrent. It is interesting that Ag/ZnO photoelectrode shows remarkably improved performance over that of ZnO in the PEC water splitting process in a mild aqueous solution ( $0.5 \text{ mol L}^{-1} \text{ Na}_2\text{SO}_4$ ) even with no applied bias. Importantly, no saturation of photocurrent density was observed on these two samples at the highest measured potential (i.e. +1.23 V versus SCE), and the increase rate of photocurrent with voltage for Ag/ZnO photoelectrodes is much higher compared to that for the ZnO. The photocurrent density at 1.23 V for Ag/ZnO architectures can reach  $60 \text{ mA cm}^{-2}$  when no bias was applied, which is about three times of that of the ZnO nanostructures and previously reported ZnO nanostructures [47,50,51]. It confirms that the photocurrent originating from the PEC water splitting can be directly correlated with the amount of hydrogen evolved.

#### 4. Conclusions

In conclusion, Ag/ZnO 3D assemblies have been designed and prepared via a facial solution method followed by low temperature calcination. The experimental results demonstrate that 3D Ag/ZnO assemblies possess higher photocurrent response and sun-light driven superior photocatalytic activities to those of pure ZnO architectures. Almost 100% photocatalytic degradation of 4-NP was obtained just for 25 min and  $0.4436 \text{ mmol g}^{-1} \text{ h}^{-1}$  of hydrogen production rate was achieved. The enhanced photocatalytic activity can be attributed to their unique assembled structures and the 2D Ag/ZnO porous single crystalline nanosheet building blocks. The Ag/ZnO assemblies have applications in the fields of photocatalytic degradation of extensive organic pollutants as well as photocatalytic and PEC water splitting hydrogen evolution. Hence, precisely designed Ag/ZnO architectures are expected to provide new avenues for the development of high performance photocatalysts having applications in hydrogen energy and environmental abatement.

#### Acknowledgements

Financial supports from the Natural Science Foundation of Shandong Province (ZR2017BM034, ZR2013BM002) and the National

Fig. 12. (a) photocurrent response (j-t curves) and (b) photocurrent density-potential (j-v) curves at a scan rate of  $5 \text{ mV s}^{-1}$  of the Ag/ZnO and ZnO photoelectrodes. These were measured without applied bias.

Natural Science Foundation of China (51272118, 51342005) are gratefully acknowledged.

#### References

- [1] W. Wang, M.O. Tade, Z.P. Shao, Chem. Soc. Rev. 44 (2015) 5371–5408.
- [2] C.L. Yu, W.Q. Zhou, H. Liu, Y. Liu, D.D. Dionysiou, Chem. Eng. J. 287 (2016) 117–129.
- [3] H.L. Wang, L.S. Zhang, Z.G. Chen, J.Q. Hu, S.J. Li, Z.H. Wang, J.S. Liu, X.C. Wang, Chem. Soc. Rev. 43 (2014) 5234–5244.
- [4] M.A. Rauf, S.S. Ashraf, Chem. Eng. J. 151 (2009) 10–18.
- [5] R. Daghrir, P. Drogui, D. Robert, Ind. Eng. Chem. Res. 52 (2013) 3581–3599.
- [6] C.E. Clarke, F. Kielar, H.M. Talbot, K.L. Johnson, Environ. Sci. Technol. 44 (2010) 1116–1122.
- [7] J. Schneider, M. Matsuoka, M. Takeuchi, J. Zhang, Y. Horiuchi, M. Anpo, D.W. Bahnemann, Chem. Rev. 114 (2014) 9919–9986.
- [8] A. Umar, M.S. Akhtar, A. Al-Hajry, M.S. Al-Assiri, G.N. Dar, M.S. Islam, Chem. Eng. J. 262 (2015) 588–596.
- [9] L.V. Trandafilović, D.J. Jovanović, X. Zhang, S. Ptasińska, M.D. Dramićanin, Appl. Catal. B: Environ. 203 (2017) 740–752.
- [10] W.L. Yu, J.F. Zhang, T.Y. Peng, Appl. Catal. B: Environ. 181 (2016) 220–227.
- [11] D.L. Li, R.L. Li, M.M. Lu, X.Y. Lin, Y.Y. Zhang, L.L. Jiang, Appl. Catal. B: Environ. 200 (2017) 566–577.
- [12] G. Nuray, O. Mahmud, Int. J. Hydrogen Energy 41 (2016) 20100–20112.
- [13] X. Liu, W.B. Li, N. Chen, Y.D. Wang, RSC Adv. 5 (2015) 34456–34465.
- [14] J. Liu, Z.Y. Hu, Y. Peng, H.W. Huang, Y. Li, M. Wu, X.X. Ke, G.V. Tendeloo, B.L. Su, Appl. Catal. B 181 (2016) 138–145.
- [15] M.J. Sampaio, M.J. Lima, D.L. Baptista, A.M.T. Silva, C.G. Silva, J.L. Faria, Chem. Eng. J. 318 (2017) 95–102.
- [16] Y. Cheng, L. An, J. Lan, F. Gao, R. Tan, X.M. Li, G.H. Wang, Mater. Res. Bull. 48 (2013) 4287–4293.
- [17] W.W. Lu, S.Y. Gao, J.J. Wang, J. Phys. Chem. C 112 (2008) 16792–16800.
- [18] Z.Z. Han, L.L. Ren, Z.H. Cui, C.Q. Chen, H.B. Pan, J.Z. Chen, Appl. Catal. B: Environ. 126 (2012) 298–305.
- [19] X.D. Zhang, Y.X. Wang, F.L. Hou, H.X. Li, Y. Yang, X.X. Zhang, Y.Q. Yang, Y. Wang, Appl. Surf. Sci. 391 (2017) 476–483.
- [20] Y.M. Liang, N. Guo, L.L. Li, R.Q. Li, G.J. Ji, S.C. Gan, New J. Chem. 40 (2016) 1587–1594.
- [21] J.F. Xie, X.D. Zhang, H. Zhang, J.J. Zhang, S. Li, R.X. Wang, B.C. Pan, Y. Xie, Adv. Mater. 29 (2017) 1604765.
- [22] X.C. Jiao, Z.W. Chen, X.D. Li, Y.F. Sun, S. Gao, W.S. Yan, C.M. Wang, Q. Zhang, Y. Lin, Y. Luo, Y. Xie, J. Am. Chem. Soc. 139 (2017) 7586–7594.
- [23] W.W. Lu, S.Y. Gao, J.J. Wang, J. Phys. Chem. C 112 (2008) 16792–16800.
- [24] J. Wang, Y. Xia, H.Y. Zhao, G.F. Wang, L. Xiang, J.L. Xu, Appl. Catal. B 206 (2017) 406–416.
- [25] C.Q. Chen, Y.H. Zheng, Y.Y. Zhan, X.Y. Lin, Q. Zheng, K.M. Wei, Dalton Trans. 40 (2011) 9566–9570.
- [26] C.D. Gu, C. Cheng, H.Y. Huang, T.L. Wong, N. Wang, T.Y. Zhang, Cryst. Growth Des. 9 (2009) 3278–3285.
- [27] Y.J. Sun, Z.T. Zhao, G. Li, P.W. Li, W.D. Zhang, Z.T. Han, K. Lian, J. Hu, Appl. Phys. A 123 (2017) 116–124.
- [28] Y.M. Liang, N. Guo, L.L. Li, R.Q. Li, G.J. Ji, S.C. Gan, Appl. Surf. Sci. 332 (2015) 32–39.
- [29] R.K. Sahu, K. Ganguly, T. Mishra, M. Mishra, R.S. Ningthoujam, S.K. Roy, L.C. Pathak, J. Colloid Interface Sci. 366 (2012) 8–15.
- [30] Z.W. Deng, M. Chen, G.X. Gu, L.M. Wu, J. Phys. Chem. B 112 (2007) 16–22.
- [31] Q. Deng, X.W. Duan, H.L. NgDickon, H.B. Tang, Y. Yang, M.G. Kong, Z.K. Wu, W.P. Cai, G.Z. Wang, ACS Appl. Mater. Interfaces 4 (2012) 6030–6037.
- [32] H.S. Mona, A.K. Tahereh, M. Fatemeh, RSC Adv. 5 (2015) 9050–9056.
- [33] D.B. Wang, C.X. Song, Z.S. Hu, Cryst. Res. Technol. 43 (2008) 55–60.
- [34] Z.Z. Han, L.L. Ren, Z.H. Cui, C.Q. Chen, H.B. Pan, J.Z. Chen, Appl. Catal. B 126 (2012) 298–305.
- [35] S. Wang, Y. Yu, Y. Zuo, C. Li, J. Yang, C. Lu, Nanoscale 4 (2012) 5895–5901.
- [36] P. Chhetri, K.K. Barakoti, M.A. Alpuche-Aviles, J. Phys. Chem. C 119 (2015) 1506–1516.
- [37] H.J. Chen, G. Liu, L.Z. Wang, Sci. Rep. 5 (2015) 10852.

- [38] H. Usui, J. Phys. Chem. C 111 (2007) 9060–9065.
- [39] X.C. Jiao, Z.W. Chen, X.D. Li, Y.F. Sun, S. Gao, W.S. Yan, C.M. Wang, Q. Zhang, Y. Lin, Y. Luo, Y. Xie, J. Am. Chem. Soc. 139 (2017) 7586–7594.
- [40] L. Zhang, W.Z. Wang, D. Jiang, E.P. Gao, S.M. Sun, Nano. Res. 8 (2015) 821–831.
- [41] R. Georgekutty, M.K. Seery, S.C. Pillai, J. Phys. Chem. C 112 (2008) 13563–13570.
- [42] Q. Deng, H.B. Tang, G. Liu, X.P. Song, G.P. Xu, Q. Li, H.L. NgDickon, G.Z. Wang, Appl. Surf. Sci. 331 (2015) 50–57.
- [43] P. Luan, M.Z. Xie, X.D. Fu, Y. Qu, X.J. Sun, L.Q. Jing, Phys. Chem. Chem. Phys. 17 (2015) 5043–5050.
- [44] H.R. Liu, Y.C. Hu, Z.X. Zhang, X.G. Liu, H.S. Jia, B.S. Xu, Appl. Surf. Sci. 355 (2015) 644–652.
- [45] M.J. Sampaio, J.W.L. Oliveira, C.I.L. Sombrio, J.L. Faria, Appl. Catal. A 518 (2016) 198–205.
- [46] D. Bao, P. Gao, X.Y. Zhu, S.C. Sun, Y. Wang, X.B. Li, Y.J. Chen, H. Zhou, Y.B. Wang, P.P. Yang, Chem. Eur. J. 21 (2015) 12728–12734.
- [47] X.Y. Zhan, Q.S. Wang, F.M. Wang, Y.J. Wang, Z.X. Wang, J.L. Cao, M. Safdar, J. He, ACS Appl. Mater. Interfaces 6 (2014) 2878–2883.
- [48] A.L. Linsebigler, G. Lu, J.T. Yates Jr., Chem. Rev. 95 (1995) 735–758.
- [49] S.K. Cushing, J.T. Li, F.K. Meng, T.R. Senty, S. Suri, M.J. Zhi, M. Li, A.D. Bristow, N.Q. Wu, J. Am. Chem. Soc. 134 (2012) 15033–15041.
- [50] X. Sun, Q. Li, J.C. Jiang, Y.B. Mao, Nanoscale 6 (2014) 8769–8780.
- [51] Q. Li, X. Sun, K. Lozano, Y.B. Mao, J. Phys. Chem. C 118 (2014) 13467–13475.